Electronic Research Archive

https://www.aimspress.com/journal/era

ERA, 32(11): 6481–6502.
DOI: 10.3934/era.2024303
Received: 21 August 2024
Revised: 12 November 2024
Accepted: 19 November 2024
Published: 29 November 2024

Research article

On fast reconstruction of periodic structures with partial scattering data

John Daugherty[1], Nate Kaduk[2], Elena Morgan[3], Dinh-Liem Nguyen[4,*], Peyton Snidanko[5] and Trung Truong[6]

[1] College of Professional Programs, Southwest Baptist University, Bolivar, MO 65613, USA
[2] Department of Mathematical Sciences, Kent State University, Kent, OH 44240, USA
[3] Department of Mathematics, Marist College, Poughkeepsie, NY 12601, USA
[4] Department of Mathematics, Kansas State University, Manhattan, KS 66506, USA
[5] Department of Mathematics, Bradley University, Peoria, IL 61625, USA
[6] Department of Mathematics and Physics, Marshall University, Huntington, WV 25755, USA

* **Correspondence:** Email: dlnguyen@ksu.edu.

Abstract: This paper presents a numerical method for solving the inverse problem of reconstructing the shape of periodic structures from scattering data. This inverse problem is motivated by applications in the nondestructive evaluation of photonic crystals. The numerical method belongs to the class of sampling methods that aim to construct an imaging function for the shape of the periodic structure using scattering data. By extending the results of Nguyen, Stahl, and Truong [Inverse Problems, 39:065013, 2023], we studied a simple imaging function that uses half the data required by the numerical method in the cited paper. Additionally, this imaging function is fast, simple to implement, and very robust against noise in the data. Both isotropic and anisotropic cases were investigated, and numerical examples were presented to demonstrate the performance of the numerical method.

Keywords: inverse scattering; periodic structure; imaging function; partial data

1. Introduction

We consider the inverse scattering problem for two-dimensional periodic structures which are assumed to be unboundedly periodic in the horizontal direction and bounded in the vertical direction. These periodic strutures are motivated by one-dimensional photonic crystals [1]. The inverse scattering problem of interest aims to reconstruct the shape of these periodic structures from boundary scattering data. This inverse problem is motivated by applications of nondestructive testing for photonic crystals.

During the past two decades, there has been a considerable amount of research on numerical methods for this inverse problem, see [2–11]. A significant portion of these studies involves the factorization

method [12]. This method, which belongs to the class of sampling or qualitative methods, was introduced by D. Colton and A. Kirsch [13, 14]. The factorization method aims to construct a necessary and sufficient characterization of the unknown scatterer from multi-static scattering data. It is a fast and non-iterative method that does not require advanced a priori information about the unknown scatterers. However, it is not very robust against noise in the data when imaging periodic structures [2]. For periodic scattering structures modeled by a smooth periodic function multiplied by a small surface deformation parameter, the near-field imaging method [3, 15] can provide reconstruction with super resolution.

Inspired by the direct or orthogonality sampling methods [16–19], a sampling method with novel imaging functions has been recently developed in [20,21] for imaging periodic structures from scattering data. Similar to the direct sampling method, this new sampling method is fast, stable, and simple to implement, avoiding the need to solve an ill-posed problem. Numerical studies also show that this method is more accurate than the direct sampling method and more stable than the factorization method for imaging periodic structures. This paper extends the results in [20]. Specifically, we modify the imaging function developed in [20] to use only half the data required by the original imaging function. Additionally, this imaging function is fast, simple to implement, and very robust against noise in the data. We study the modified imaging function for both isotropic and anisotropic cases of periodic scattering media. Numerical examples are presented to demonstrate the performance of the numerical method and to compare it with the direct sampling method and the factorization method.

The paper is organized as follows. The basics of the scattering from periodic media and the inverse problem of interest are described in Section 2. The modified imaging function and its analysis for the isotropic case are discussed in Section 3. Results for the case of anisotropic media are presented in Section 4. Finally, Section 5 is dedicated to a numerical study of the sampling method and its comparison to the factorization method and the orthogonality sampling method.

2. Problem setup

We consider a two-dimensional medium that is 2π periodic in the x_1-direction and bounded in the x_2-direction. While we choose the period to be 2π for convenience, the medium can have any arbitrary period. For $\alpha \in \mathbb{R}$, a function $f : \mathbb{R}^2 \to \mathbb{C}$ is α-quasiperiodic in x_1 if

$$f(x_1 + 2\pi j, x_2) = e^{i2\pi j\alpha} f(x_1, x_2), \quad \forall j \in \mathbb{Z}.$$

Let $q : \mathbb{R}^2 \to \mathbb{R}$ be a bounded function that represents the material parameter of the medium relative to that of the background. Assume that q is 2π-periodic in x_1, supp(q) is bounded in x_2, and $q = 0$ outside of the medium. We consider an α-quasiperiodic incident field, u_{in}, to illuminate the medium. The medium scatters the incident field and produces a scattered field, u_{sc}, which satisfies the Helmholtz equation,

$$\Delta u_{sc} + k^2 u_{sc} = -k^2 q u \quad \text{in } \mathbb{R}^2, \tag{2.1}$$

where $u := u_{sc} + u_{in}$ is the total field, and $k > 0$ is the wave number. It is well known that u_{sc} is also α-quasiperiodic in x_1. Thus, the problem can be reduced to one period:

$$\Omega := (-\pi, \pi) \times \mathbb{R}.$$

Let $D := \text{supp}(q) \cap \Omega$ and $h > 0$ such that

$$h > \sup\{|x_2| : x = (x_1, x_2) \in D\}. \tag{2.2}$$

To ensure that the direct scattering problem is well-posed, we impose the Rayleigh radiation condition for the scattered field as

$$u_{sc}(x) = \begin{cases} \sum_{j\in\mathbb{Z}} u_j^+ e^{i\alpha_j x_1 + i\beta_j(x_2-h)}, & x_2 \geq h, \\ \sum_{j\in\mathbb{Z}} u_j^- e^{i\alpha_j x_1 - i\beta_j(x_2+h)}, & x_2 \leq -h, \end{cases} \tag{2.3}$$

where

$$\alpha_j := \alpha + j, \quad \beta_j := \begin{cases} \sqrt{k^2 - \alpha_j^2}, & k^2 > \alpha_j^2 \\ i\sqrt{\alpha_j^2 - k^2}, & k^2 < \alpha_j^2 \end{cases} \qquad j \in \mathbb{Z},$$

and $u_j^\pm$, $j \in \mathbb{Z}$, are called the Rayleigh coefficients of the scattered field. The condition (2.3) means that u_{sc} is an outgoing wave. Note that we exclude the case where $k = \alpha_j$ for some j, which is known as Wood's anomaly. See [22] for a detailed discussion on well-posedness of the direct problem under some assumption on q and wave number k. For the study of the inverse problem of this paper, we will assume that the direct problem (2.1)–(2.3) is well-posed. Let

$$\Gamma_{\pm h} := (-\pi, \pi) \times \{\pm h\},$$

and the inverse problem of interest can be stated as follows.

Inverse problem: Using multiple incident fields at a fixed wave number k to illuminate an unknown scattering medium, determine the geometry D of the medium from the measurement of the scattered fields on either Γ_{+h} or Γ_{-h}.

To solve this inverse problem, we introduce a new imaging function, which is inspired by that for the case of full measurement on $\Gamma_{+h} \cup \Gamma_{-h}$ in [20].

3. The imaging function and its properties

For $N \in \mathbb{N}$ and $l = 1, 2, \ldots, N$, we denote by $u_{in}(x, l)$ the incident fields used to illuminate the unknown medium. The corresponding scattered fields and total fields are denoted by $u_{sc}(x, l)$ and $u(x, l)$, respectively. It is well-known that the scattered fields satisfy the Lippmann-Schwinger integral equation [23]:

$$u_{sc}(x, l) = k^2 \int_D G(x, y) q(y) u(y, l) dy, \tag{3.1}$$

where $G(x, y)$ is the α-quasiperiodic Green's function, which admits the following series representation [1]:

$$G(x, y) := \frac{i}{4\pi} \sum_{j\in\mathbb{Z}} \frac{1}{\beta_j} e^{i\alpha_j(x_1-y_1)+i\beta_j|x_2-y_2|}, \quad x, y \in \Omega, x \neq y. \tag{3.2}$$

Note that $G(\cdot, y)$ also admits a Rayleigh expansion similar to (2.3), and its Rayleigh coefficients $g_j^\pm(y)$ are given by

$$g_j^\pm(y) = \frac{i}{4\pi\beta_j} e^{-i\alpha_j y_1 \mp i\beta_j(y_2 \mp h)}. \tag{3.3}$$

Now, let us discuss the following lemma, which is the motivation behind the definition of the imaging function.

Lemma 1. *Let* $\Omega_h := (-\pi, \pi) \times (-h, h)$ *and*

$$F(x, y) := \frac{G(x, y) - \overline{G(y, x)}}{2i}.$$

Then, for $x \in \Gamma_{+h} \cup \Gamma_{-h}$ *and* $y \in \Omega_h$,

$$F(x, y) = \frac{1}{8\pi^2} \sum_{j:\beta_j>0} \frac{1}{\beta_j} e^{i\alpha_j(x_1-y_1)} \cos(\beta_j(x_2 - y_2)).$$

Moreover, for $y, z \in \Omega_h$,

$$\int_{\Gamma_{+h}\cup\Gamma_{-h}} \frac{\partial F(x, y)}{\partial \nu(x)} \overline{G(x, z)} - F(x, y) \frac{\partial \overline{G(x, z)}}{\partial \nu(x)} \, ds(x) = F(z, y), \tag{3.4}$$

where $\nu(x)$ *denotes the normal vector.*

Proof. For $x \in \Gamma_{+h}$ and $y \in \Omega_h$, we have $x_2 > y_2$ and

$$G(x, y) = \frac{i}{4\pi} \sum_{j\in\mathbb{Z}} \frac{1}{\beta_j} e^{i\alpha_j(x_1-y_1)+i\beta_j(x_2-y_2)}, \tag{3.5}$$

$$\overline{G(y, x)} = \frac{-i}{4\pi} \sum_{j\in\mathbb{Z}} \frac{1}{\overline{\beta_j}} e^{-i\alpha_j(y_1-x_1)-i\overline{\beta_j}(x_2-y_2)}.$$

From these two expressions, we can see that the terms for which β_j is complex-valued in $G(x, y)$ coincide with their counterparts in $\overline{G(y, x)}$. Thus,

$$\begin{aligned} F(x, y) &= \frac{1}{8\pi} \sum_{j:\beta_j>0} \frac{1}{\beta_j} e^{i\alpha_j(x_1-y_1)} \left(e^{i\beta_j(x_2-y_2)} + e^{-i\beta_j(x_2-y_2)} \right) \\ &= \frac{1}{4\pi} \sum_{j:\beta_j>0} \frac{1}{\beta_j} e^{i\alpha_j(x_1-y_1)} \cos(\beta_j(x_2 - y_2)). \end{aligned}$$

Next, for fixed $z, y \in \Omega_h$,

$$\begin{aligned} &\int_{\Gamma_{+h}} \frac{\partial F(x, y)}{\partial \nu} \overline{G(x, z)} - F(x, y) \frac{\partial \overline{G(x, z)}}{\partial \nu} \, ds(x) \\ &= \frac{i}{16\pi^2} \int_{\Gamma_{+h}} \sum_{j:\beta_j>0} e^{i\alpha_j(x_1-y_1)} \sin(\beta_j(x_2 - y_2)) \sum_{j\in\mathbb{Z}} \frac{1}{\overline{\beta_j}} e^{-i\alpha_j(x_1-z_1)-i\overline{\beta_j}(x_2-z_2)} \, ds(x) \\ &+ \frac{1}{16\pi^2} \int_{\Gamma_{+h}} \sum_{j:\beta_j>0} \frac{1}{\beta_j} e^{i\alpha_j(x_1-y_1)} \cos(\beta_j(x_2 - y_2)) \sum_{j\in\mathbb{Z}} e^{-i\alpha_j(x_1-z_1)-i\overline{\beta_j}(x_2-z_2)} \, ds(x) \\ &= \frac{i}{16\pi^2} \sum_{j_1:\beta_{j_1}>0} \sum_{j_2\in\mathbb{Z}} \frac{1}{\overline{\beta_{j_2}}} \sin(\beta_{j_1}(h - y_2)) e^{-i\overline{\beta_{j_2}}(h-z_2)} e^{i\alpha_{j_2}z_1-i\alpha_{j_1}y_1} \int_{-\pi}^{\pi} e^{i(j_1-j_2)x_1} \, dx_1 \\ &+ \frac{1}{16\pi^2} \sum_{j_1:\beta_{j_1}>0} \sum_{j_2\in\mathbb{Z}} \frac{1}{\beta_{j_1}} \cos(\beta_j(h - y_2)) e^{-i\overline{\beta_{j_2}}(h-z_2)} e^{i\alpha_{j_2}z_1-i\alpha_{j_1}y_1} \int_{-\pi}^{\pi} e^{i(j_1-j_2)x_1} \, dx_1. \end{aligned}$$

Note that

$$\int_{-\pi}^{\pi} e^{i(j_1-j_2)x_1}\,dx_1 = \begin{cases} 2\pi & \text{if } j_1 = j_2, \\ 0 & \text{if } j_1 \neq j_2, \end{cases} \tag{3.6}$$

and therefore,

$$\begin{aligned}\int_{\Gamma_{+h}} \frac{\partial F(x,y)}{\partial \nu}\overline{G(x,z)} - F(x,y)\frac{\partial \overline{G(x,z)}}{\partial \nu}\,ds(x) &= \frac{i}{8\pi}\sum_{j:\beta_j>0}\frac{1}{\beta_j}\sin(\beta_j(h-y_2))e^{-i\beta_j(h-z_2)}e^{i\alpha_j(z_1-y_1)} \\ &\quad + \frac{1}{8\pi}\sum_{j:\beta_j>0}\frac{1}{\beta_j}\cos(\beta_j(h-y_2))e^{-i\beta_j(h-z_2)}e^{i\alpha_j(z_1-y_1)} \\ &= \frac{1}{8\pi}\sum_{j:\beta_j>0}\frac{1}{\beta_j}e^{i\alpha_j(z_1-y_1)+i\beta_j(z_2-y_2)}.\end{aligned}$$

Similarly, for $x \in \Gamma_{-h}$ and $y \in \Omega_h$, we have $x_2 < y_2$, and we can show that

$$F(x,y) = \frac{1}{8\pi^2}\sum_{j:\beta_j>0}\frac{1}{\beta_j}e^{i\alpha_j(z_1-y_1)}\cos(\beta_j(z_2-y_2)).$$

Moreover, by the same reasoning, we can also show that

$$\int_{\Gamma_{-h}} \frac{\partial F(x,y)}{\partial \nu}\overline{G(x,z)} - F(x,y)\frac{\partial \overline{G(x,z)}}{\partial \nu}\,ds(x) = \frac{1}{8\pi}\sum_{j:\beta_j>0}\frac{1}{\beta_j}e^{i\alpha_j(z_1-y_1)-i\beta_j(z_2-y_2)}.$$

Therefore,

$$\begin{aligned}&\int_{\Gamma_{+h}\cup\Gamma_{-h}} \frac{\partial F(x,y)}{\partial \nu}\overline{G(x,z)} - F(x,y)\frac{\partial \overline{G(x,z)}}{\partial \nu}\,ds(x) \\ &= \frac{1}{8\pi}\sum_{j:\beta_j>0}\left(e^{i\alpha_j(z_1-y_1)+i\beta_j(z_2-y_2)} + e^{i\alpha_j(z_1-y_1)-i\beta_j(z_2-y_2)}\right) \\ &= \frac{1}{4\pi}\sum_{j:\beta_j>0}\frac{1}{\beta_j}e^{i\alpha_j(z_1-y_1)}\cos(\beta_j(z_2-y_2)) = F(z,y).\end{aligned}$$

The reason why (3.4) helps us define the imaging function is as follows. Using the Rayleigh expansion of the Green's function, the left-hand side of (3.4) becomes

$$\int_{\Gamma_{+h}\cup\Gamma_{-h}} \frac{\partial F(x,y)}{\partial \nu}\overline{G(x,z)} - F(x,y)\frac{\partial \overline{G(x,z)}}{\partial \nu}\,ds(x) = 2\pi\sum_{j:\beta_j>0}\beta_j\left(\overline{g_j^+(z)}g_j^+(y) + \overline{g_j^-(z)}g_j^-(y)\right).$$

Then, as done in [20], we can show that

$$2\pi\sum_{j:\beta_j>0}\beta_j\left(\overline{g_j^+(z)}u_j^+(l) + \overline{g_j^-(z)}u_j^-(l)\right) = k^2\int_D F(z,y)q(y)u(y,l)\,dy.$$

So, if we define the imaging function as

$$\mathcal{I}(z) := \sum_{l=1}^{N} \left| \sum_{j:\beta_j>0} \beta_j \left(\overline{g_j^+(z)} u_j^+(l) + \overline{g_j^-(z)} u_j^-(l) \right) \right|^p ,$$

we would have

$$\mathcal{I}(z) = \sum_{l=1}^{N} \left| \frac{k^2}{2\pi} \int_D F(z,y) q(y) u(y,l)\, dy \right|^p .$$

From this equation, we can expect the imaging function to exhibit behaviors similar to the kernel $F(z,y)$. We will discuss this in detail shortly. In the case of data measured on either Γ_{+h} or Γ_{-h}, we will only have either u_j^+ or u_j^-, respectively. A natural way to modify the imaging function is to omit the term for which data is not available. For example, when data is measured only on Γ_+, the term $\overline{g_j^-(z)} u_j^-(l)$ will be dropped.

For $z \in \Omega_h$, we define the (general) imaging function $\mathcal{I}(z)$ as

$$\mathcal{I}(z) := \sum_{l=1}^{N} \left| \sum_{j:\beta_j>0} \beta_j \left(\chi^+(t) u_j^+(l) \overline{g_j^+(z)} + \chi^-(t) u_j^-(l) \overline{g_j^-(z)} \right) \right|^p , \tag{3.7}$$

where $p \in \mathbb{N}$ is used to sharpen the resolution of the imaging function, $t \in \{\mathrm{U}, \mathrm{L}, \mathrm{B}\}$ (abbreviations for Upper, Lower, and Both), and

$$\chi^+(t) = \begin{cases} 1, & \text{for } t = \mathrm{U}, \mathrm{B} \\ 0, & \text{for } t = \mathrm{L} \end{cases}, \quad \chi^-(t) = \begin{cases} 1, & \text{for } t = \mathrm{L}, \mathrm{B} \\ 0, & \text{for } t = \mathrm{U}. \end{cases}$$

The choice of t here allows the imaging function to apply to scattering data measured on either one side (Upper or Lower) or both sides (Both) of the periodic structures. The imaging function defined above satisfies the following property.

Theorem 2. *For all $z \in \Omega_h$, the imaging function $\mathcal{I}(z)$ satisfies*

$$\mathcal{I}(z) = \sum_{l=1}^{N} \left| k^2 \int_D F_t(z,y) q(y) u(y,l) dy \right|^p$$

where

$$F_t(z,y) = \begin{cases} \dfrac{1}{16\pi^2} \displaystyle\sum_{j:\beta_j>0} \frac{1}{\beta_j} e^{i\alpha_j(z_1-y_1)+i\beta_j(z_2-y_2)} & \text{if } t = U, \\ \dfrac{1}{16\pi^2} \displaystyle\sum_{j:\beta_j>0} \frac{1}{\beta_j} e^{i\alpha_j(z_1-y_1)-i\beta_j(z_2-y_2)} & \text{if } t = L, \\ \dfrac{1}{8\pi^2} \displaystyle\sum_{j:\beta_j>0} \frac{1}{\beta_j} e^{i\alpha_j(z_1-y_1)} \cos(\beta_j(z_2-y_2)) & \text{if } t = B. \end{cases} \tag{3.8}$$

Remark 3. *Graphical observations display that the kernel functions (3.8) exhibit a peak when $z \approx y$ and decay rapidly as z and y are apart from each other. Moreover, this peak becomes more distinct with larger values of k, as shown in Figure 1.*

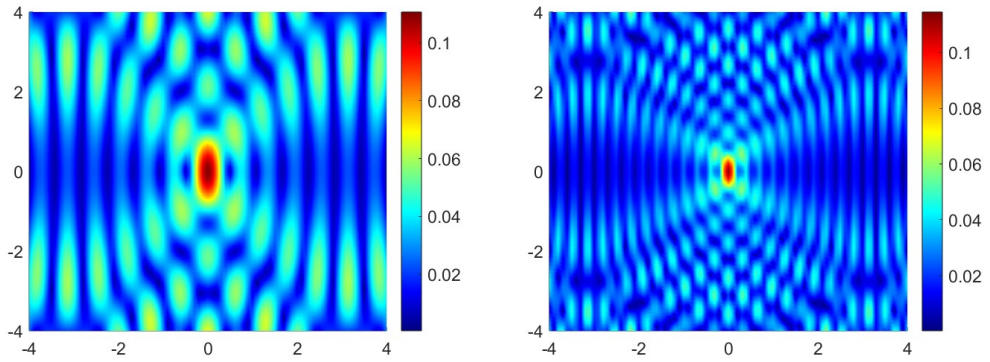

(a) $k = 5.5$ **(b)** $k = 10.5$

Figure 1. The values of $|F_U(z, 0)|$ for $\alpha = 0$.

The behavior of the kernel can be justified in some simple cases. For example, in the context of near-field measurements, where $\Gamma_{\pm h}$ are very close to periodic scatterer D, we can reasonably assume that $z_2 \approx y_2$. Furthermore, if we consider $\alpha \approx 0$ in the incident field, the kernel $F_U(z, y)$ simplifies to

$$F_U(z, y) \approx \frac{1}{16\pi^2} \sum_{j:|j|<k} \frac{e^{ij(z_1-y_1)}}{\sqrt{k^2 - j^2}} = \frac{1}{16\pi^2 k} + \frac{1}{8\pi^2} \sum_{1\le j<k} \frac{\cos(j(z_1 - y_1))}{\sqrt{k^2 - j^2}}.$$

When $z_1 = y_1$, the terms $\cos(j(z_1 - y_1))$ all reach their maximum value simultaneously. However, for $z_1 \neq y_1$, these terms also have other maxima, but they no longer align at the same point as j varies, since the periods of the cosine functions differ. Therefore, $F_U(z, y)$ will have a larger value when $z \approx y$. As z moves farther from y, the cosine terms are more likely to differ in sign at z, leading to cancellations in their sum. As a result, $F(z, y)$ becomes significantly smaller. A larger k results in the summation of more maximal values when $z \approx y$ and more cancellations as z and y are apart from each other. Thus, the peak of $F_U(z, y)$ appears more distinct for larger k, as illustrated in Figure 1. This justification certainly applies to $F_t(z, y)$ for $t = L$ or $t = B$. Based on the behavior of $F_t(z, y)$, we expect $\mathcal{I}(z)$ to take relatively small values when z is outside D and significantly larger values when z is inside D.

It is worth noting that Theorem 2 can be proved using the integral representation (3.4) by following a similar approach as in [20]. However, in this paper, we propose an alternative simple proof. This proof does not rely on Green's identities, which allows us to study the imaging function using scattering data measured from only one side of the periodic structure.

Proof. **Case t = U.** Note that the Rayleigh coefficients of the scattered field satisfy

$$u_j^+(l) = \frac{1}{2\pi} \int_{\Gamma_{+h}} u_{sc}(x, l) e^{-i\alpha_j x_1} ds(x). \tag{3.9}$$

Substituting the Lippmann-Schwinger equation (3.1) into the integral (3.9) gives

$$u_j^+(l) = \frac{1}{2\pi} \int_{\Gamma_{+h}} \Big(k^2 \int_D G_{k,\alpha}(x, y) q(y) u(y, l) dy\Big) e^{-i\alpha_j x_1} ds(x).$$

Note that the integrand is bounded and D and Γ_{+h} are bounded sets. Therefore, by Fubini's theorem,

$$\begin{aligned} u_j^+(l) &= k^2 \int_D \left(\frac{1}{2\pi} \int_{\Gamma_{+h}} G_{k,\alpha}(x,y) e^{-i\alpha_j x_1} \, ds(x) \right) q(y) u(y,l) dy \\ &= k^2 \int_D g_j^+(y) q(y) u(y,l) dy. \end{aligned}$$

Plugging this into the definition of $\mathcal{I}(z)$ gives

$$\begin{aligned} \mathcal{I}(z) &= \sum_{l=1}^N \left| \sum_{j:\beta_j>0} \beta_j \overline{g_j^+(z)} u_j^+(l) \right|^p \\ &= \sum_{l=1}^N \left| k^2 \int_D \left(\sum_{j:\beta_j>0} \beta_j \overline{g_j^+(z)} g_j^+(y) \right) q(y) u(y,l) dy \right|^p. \end{aligned}$$

By (3.3), for j such that $\beta_j > 0$,

$$\begin{aligned} \overline{g_j^+(z)} g_j^+(y) &= \frac{1}{16\pi^2\beta_j^2} e^{i\alpha_j z_1 + i\beta_j(z_2-h)} e^{-i\alpha_j y_1 - i\beta_j(y_2-h)} \\ &= \frac{1}{16\pi^2\beta_j^2} e^{i\alpha_j(z_1-y_1)+i\beta_j(z_2-y_2)}. \end{aligned}$$

Therefore,

$$\sum_{j:\beta_j>0} \beta_j \overline{g_j^+(z)} g_j^+(y) = \frac{1}{16\pi^2} \sum_{j:\beta_j>0} \frac{1}{\beta_j} e^{i\alpha_j(z_1-y_1)+i\beta_j(z_2-y_2)} = F_U(z,y), \tag{3.10}$$

and thus,

$$\mathcal{I}(z) = \sum_{l=1}^N \left| k^2 \int_D F_U(z,y) q(y) u(y,l) dy \right|^p.$$

Case t = L. By similar reasoning, we can show that

$$\sum_{j:\beta_j>0} \beta_j \overline{g_j^-(z)} g_j^-(y) = F_L(z,y) \tag{3.11}$$

and

$$u_j^-(l) = k^2 \int_D g_j^-(y) q(y) u(y,l) dy,$$

and the result then follows.

Case t = B. Adding (3.10) and (3.11) together gives

$$\sum_{j:\beta_j>0} \beta_j \left(\overline{g_j^+(z)} g_j^+(y) + \overline{g_j^-(z)} g_j^-(y) \right) = F_U(z,y) + F_L(z,y) = F_B(z,y).$$

Therefore,

$$\mathcal{I}(z) = \sum_{l=1}^{N} \left| \sum_{j:\beta_j>0} \beta_j \left(\overline{g_j^+(z)} u_j^+(l) + \overline{g_j^-(z)} u_j^-(l) \right) \right|^p$$
$$= \sum_{l=1}^{N} \left| k^2 \int_D F_B(z,y) q(y) u(y,l) dy \right|^p .$$

Theorem 2 and Remark 3 partly justify the resolution of the imaging function $\mathcal{I}(z)$. The next theorem shows that $\mathcal{I}(z)$ is stable with respect to noise in the data.

Theorem 4. *For $\delta > 0$, let $u_{sc,\delta}(\cdot, l)$ be the noisy scattered fields that satisfy*

$$\|u_{sc,\delta}(\cdot, l) - u_{sc}(\cdot, l)\|_{L^2(\Gamma_{+h} \cup \Gamma_{-h})} \leq \delta \|u_{sc}(\cdot, l)\|_{L^2(\Gamma_{+h} \cup \Gamma_{-h})}, \quad \text{for all } l = 1, 2, \ldots, N,$$

and let $u_{j,\delta}^{\pm}(l)$ be the corresponding Rayleigh coefficients. We define $\mathcal{I}_\delta(z)$ as the imaging function as in (3.7) *where $u_j^{\pm}(l)$ are replaced by $u_{j,\delta}^{\pm}(l)$. Then, for all $z \in \Omega$, the following stability property holds:*

$$|\mathcal{I}_\delta(z) - \mathcal{I}(z)| \leq C\delta, \quad \text{as } \delta \to 0,$$

where $C > 0$ is a constant independent of z and δ.

The proof of this theorem follows a similar approach to that in [20] and is therefore omitted here. In summary, we have introduced an imaging function for reconstructing the unknown isotropic scatterer D using scattering data measured either above or below the periodic structures. We also provided partial justification for its resolution and stability. In the next section, we extend the analysis of this imaging function to the case of anisotropic media.

4. The case of anisotropic media

In the case of scattering from anisotropic media, let $Q : \mathbb{R}^2 \to \mathbb{R}^{2\times 2}$ be the material parameter of the periodic scattering medium. We assume that Q is a matrix-valued bounded function which is 2π-periodic with respect to x_1, Q is zero outside of the medium, and supp(Q) is bounded in x_2. We consider the following equation:

$$\Delta u_{sc} + k^2 u_{sc} = - \div (Q \nabla u),$$

where u_{sc} satisfies the radiation condition (2.3). We refer to [22] for results on the well-posedness of the direct problem under some assumption on Q and wave number k. As in the isotropic case, we assume that the direct problems is well-posed for the study of the inverse problem. Again we denote $D := \text{supp}(Q) \cap \Omega$ and the inverse problem is to determine D from given data of u_{sc} on Γ_{+h} or Γ_{-h}. From [24], we know that the corresponding Lippmann-Schwinger equation is given by

$$u_{sc}(x) = \div_x \int_D G(x,y) Q(y) \nabla u(y) dy. \tag{4.1}$$

To simplify the presentation, we will analyze the imaging function for the case of measured data on Γ_{+h}, and the other cases can be derived through a similar process as in the isotropic case. Recall that the imaging function for this case is

$$\mathcal{I}(z) := \sum_{l=1}^{N} \left| \sum_{j:\beta_j>0} \beta_j u_j^+(l)\overline{g_j^+(z)} \right|^p, \tag{4.2}$$

for $z \in \Omega_h$. The following theorem is an extension of Theorem 2 to anisotropic media.

Theorem 5. *The imaging function satisfies*

$$\mathcal{I}(z) = \sum_{l=1}^{N} \left| \int_D \mathbf{F}(z,y) \cdot Q(y)\nabla u(y,l)dy \right|^p, \tag{4.3}$$

where

$$\mathbf{F}(z,y) := \frac{1}{16\pi^2} \sum_{j:\beta_j>0} \frac{1}{\beta_j} \begin{bmatrix} \alpha_j \\ \beta_j \end{bmatrix} e^{i\alpha_j(z_1-y_1)+i\beta_j(z_2-y_2)}. \tag{4.4}$$

Proof. Plugging (4.1) into (3.9) gives

$$\begin{aligned}
u_j^+(l) &= \frac{1}{2\pi} \int_{\Gamma_{+h}} \div_x \left(\int_D G(x,y)Q(y)\nabla u(y,l)dy \right) e^{-i\alpha_j x_1} ds(x) \\
&= \frac{1}{2\pi} \int_{\Gamma_{+h}} \div_x \begin{bmatrix} \int_D G(x,y) \left(Q_{11}(y)\partial_{y_1} u(y,l) + Q_{12}(y)\partial_{y_2} u(y,l) \right) dy \\ \int_D G(x,y) \left(Q_{21}(y)\partial_{y_1} u(y,l) + Q_{22}(y)\partial_{y_2} u(y,l) \right) dy \end{bmatrix} e^{-i\alpha_j x_1} ds(x) \\
&= \frac{1}{2\pi} \int_{\Gamma_{+h}} \int_D \partial_{x_1} G(x,y) \left(Q_{11}(y)\partial_{y_1} u(y,l) + Q_{12}(y)\partial_{y_2} u(y,l) \right) dy\, e^{-i\alpha_j x_1} ds(x) \\
&+ \frac{1}{2\pi} \int_{\Gamma_{+h}} \int_D \partial_{x_2} G(x,y) \left(Q_{21}(y)\partial_{y_1} u(y,l) + Q_{22}(y)\partial_{y_2} u(y,l) \right) dy\, e^{-i\alpha_j x_1} ds(x).
\end{aligned}$$

Swapping the integrals, we obtain,

$$\begin{aligned}
u_j^+(l) &= \int_D \left(\frac{1}{2\pi} \int_{\Gamma_{+h}} \partial_{x_1} G(x,y) e^{-i\alpha_j x_1} ds(x) \right) \left(Q_{11}(y)\partial_{y_1} u(y,l) + Q_{12}(y)\partial_{y_2} u(y,l) \right) dy \\
&+ \int_D \left(\frac{1}{2\pi} \int_{\Gamma_{+h}} \partial_{x_2} G(x,y) e^{-i\alpha_j x_1} ds(x) \right) \left(Q_{21}(y)\partial_{y_1} u(y,l) + Q_{22}(y)\partial_{y_2} u(y,l) \right) dy.
\end{aligned}$$

Since $G(x,y)$ satisfies the radiation condition, so do $\partial_{x_1} G(x,y)$ and $\partial_{x_2} G(x,y)$, and their Rayleigh coefficients are $i\alpha_j g_j^+(y)$ and $i\beta_j g_j^+(y)$, respectively. Thus,

$$
\begin{aligned}
u_j^+(l) &= \int_D i\alpha_j g_j^+(y)\left(Q_{11}(y)\partial_{y_1}u(y,l) + Q_{12}(y)\partial_{y_2}u(y,l)\right)dy \\
&\quad + \int_D i\beta_j g_j^+(y)\left(Q_{21}(y)\partial_{y_1}u(y,l) + Q_{22}(y)\partial_{y_2}u(y,l)\right)dy \\
&= \int_D i g_j^+(y)\begin{bmatrix}\alpha_j \\ \beta_j\end{bmatrix}\cdot Q(y)\nabla u(y,l)dy.
\end{aligned}
$$

Plugging into (4.2), we obtain

$$
\begin{aligned}
\mathcal{I}(z) &= \sum_{l=1}^{N}\left|\sum_{j:\beta_j>0}\beta_j u_j^+(l)\overline{g_j^+(z)}\right|^p \\
&= \sum_{l=1}^{N}\left|\sum_{j:\beta_j>0} i\beta_j\int_D \overline{g_j^+(z)}g_j^+(y)\begin{bmatrix}\alpha_j \\ \beta_j\end{bmatrix}\cdot Q(y)\nabla u(y,l)dy\right|^p \\
&= \sum_{l=1}^{N}\left|\int_D \frac{1}{16\pi^2}\sum_{j:\beta_j>0}\frac{1}{\beta_j}\begin{bmatrix}\alpha_j \\ \beta_j\end{bmatrix}e^{i\alpha_j(z_1-y_1)+i\beta_j(z_2-y_2)}\cdot Q(y)\nabla u(y,l)dy\right|^p \\
&= \sum_{l=1}^{N}\left|\int_D \mathbf{F}(z,y)\cdot Q(y)\nabla u(y,l)dy\right|^p.
\end{aligned}
$$

This completes the proof.

The kernel $\mathbf{F}(z,y)$ has a similar behavior as $F_U(z,y)$ defined in (3.8). This means that, for any vector $v \in \mathbb{R}^2$ and $z, y \in \Omega_h$, $\mathbf{F}(z,y)\cdot v$ has a large value when $z \approx y$ and has a much smaller value when z moves away from y. Therefore, we can expect the imaging function to have a large value when the sampling point is inside the medium and a much smaller value when the sampling point moves away from the medium. We will confirm this numerically in the next section.

5. Numerical study

In this section, we present numerical results on the performance of our imaging function. We only present results for the case of transmission data, in which the incident sources are placed below the scatterer and the receivers are placed above the scatterer. Numerical results for full-aperture data can be found in [20]. We also compare our method with the orthogonality sampling method (OSM) and the factorization method (FM). Recall that the imaging function for our method is

$$
\mathcal{I}_\delta(z) = \sum_{l=1}^{N}\left|\sum_{j:\beta_j>0}\beta_j u_{\delta,j}^+(l)\overline{g_j^+(z)}\right|^p,
$$

and the imaging function of the OSM is given by

$$
\mathcal{I}_{OSM}(z) := \sum_{l=1}^{N}\left|\int_{\Gamma_{+h}} u_{sc,\delta}(x,l)\,\overline{G(x,z)}ds(x)\right|^p.
$$

For the factorization method, we employ a singular value decomposition and regularize the method by truncating all singular values that are less than 0.1. The parameters used in the simulation are as follows.

- $h = 1$, $\alpha = 0$.
- Wave number: $k = 10.5$.
- Sampling domain: $(-\pi, \pi) \times (-1, 1)$, partitioned into a grid of 128×64 sampling points.
- Number of incident sources: $N = 128$, placed on $\Gamma_{-3} = (-\pi, \pi) \times \{-3\}$.
- Number of receivers: 128, placed on $\Gamma_{+1} = (-\pi, \pi) \times \{1\}$.
- Noise level: $\delta = 20\%$. The noise is added to the scattered fields according the following model:

$$u_{sc,\delta} = u_{sc} + \delta \|u_{sc}\|_{L^2} \mathbf{n},$$

  where $\mathbf{n} : \Gamma_{+h} \to \mathbb{C}$ is the noise function whose values are random numbers such that $\|\mathbf{n}\|_{L^2} = 1$.
- Exponent of the imaging functions: $p = 5$.

We refer to [20] for a detailed study of the behavior of the imaging function for different sets of parameters, including different values of h, α, k, and δ, as well as different numbers of incident sources and receivers. The imaging function behaves similarly in the case of limited-aperture data with respect to these parameters.

To generate synthetic data for the inverse problem, we solve the direct problem using a spectral method studied in [25]. We compute the scattered fields at the receivers' location, add noise to them, and then compute the corresponding Rayleigh coefficients via (3.9). The incident fields we used are of the form

$$u_{in}(x, l) = G(x, x_l), \quad x \in \Omega_h,$$

where x_l is the receivers' location, $l = 1, \ldots, N$.

5.1. Results for isotropic media

First, we show numerical examples of some isotropic media. Recall that in this case, the medium is characterized by the function $q(x)$. In all examples, the function $q(x)$ has the form

$$q(x) = \begin{cases} 0.5 & \text{if } x \in D, \\ 0 & \text{if } x \notin D. \end{cases}$$

We consider four periodic media with four different geometries D.

Aligned ellipses (Figure 2). This medium consists of two horizontally aligned ellipses in each period. The radii of each ellipse are $\pi/4$ and 0.4.

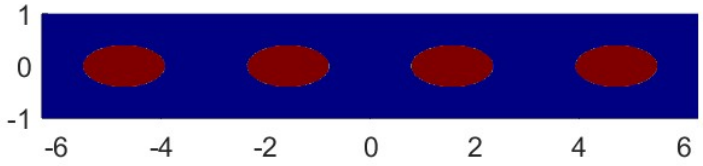

(a) True geometry

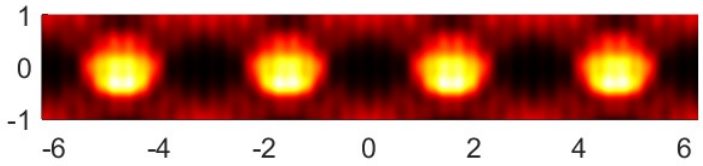

(b) Reconstruction by the proposed method

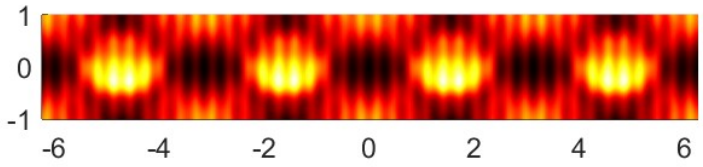

(c) Reconstruction by the OSM

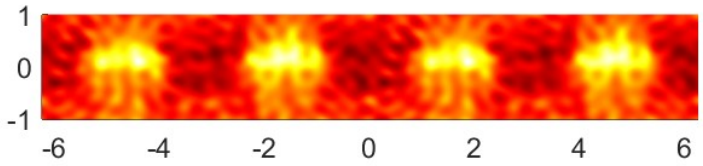

(d) Reconstruction by the FM

Figure 2. Reconstructions by the proposed method, the OSM, and the FM for the isotropic aligned ellipses.

Aligned squares (Figure 3). This medium consists of two horizontally aligned squares in each period. The side of each square is 0.4.

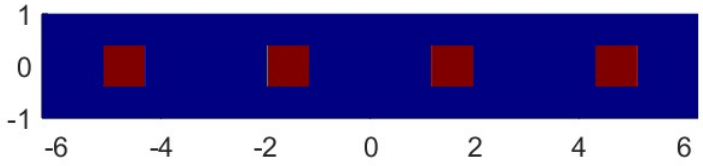

(a) True geometry

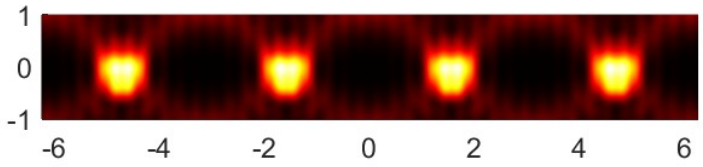

(b) Reconstruction by the proposed method

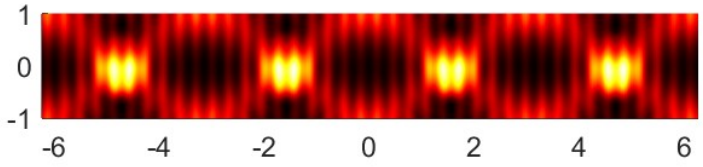

(c) Reconstruction by the OSM

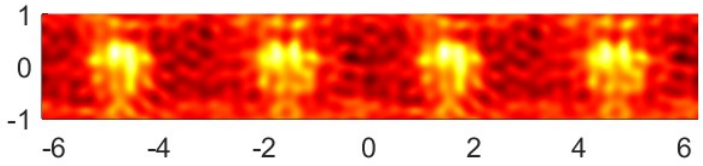

(d) Reconstruction by the FM

Figure 3. Reconstructions by the proposed method, the OSM, and the FM for the isotropic aligned squares.

Aligned crosses (Figure 4). This medium consists of two horizontally aligned crosses in each period. Each cross is made up of one horizontal 0.55×0.18 rectangle and vertical 0.18×0.45 rectangle.

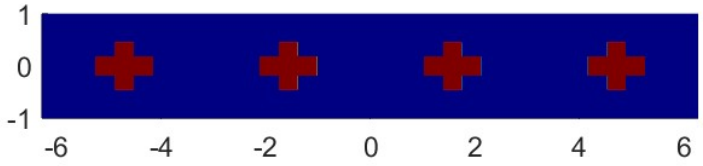

(a) True geometry

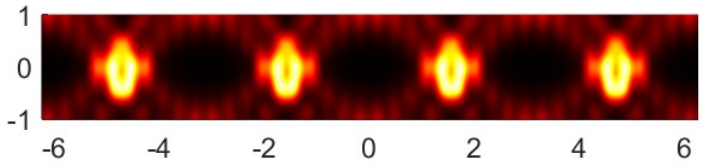

(b) Reconstruction by the proposed method

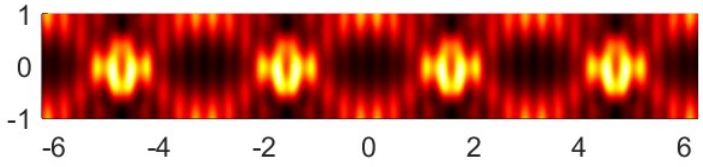

(c) Reconstruction by the OSM

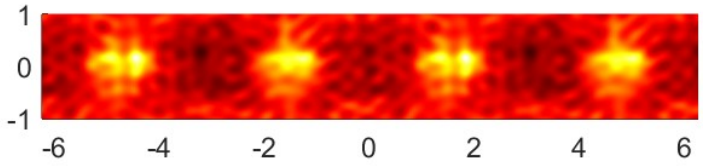

(d) Reconstruction by the FM

Figure 4. Reconstructions by the proposed method, the OSM, and the FM for the isotropic crosses.

Aligned kites (Figure 5). This medium consists of a kite-shaped object in each period.

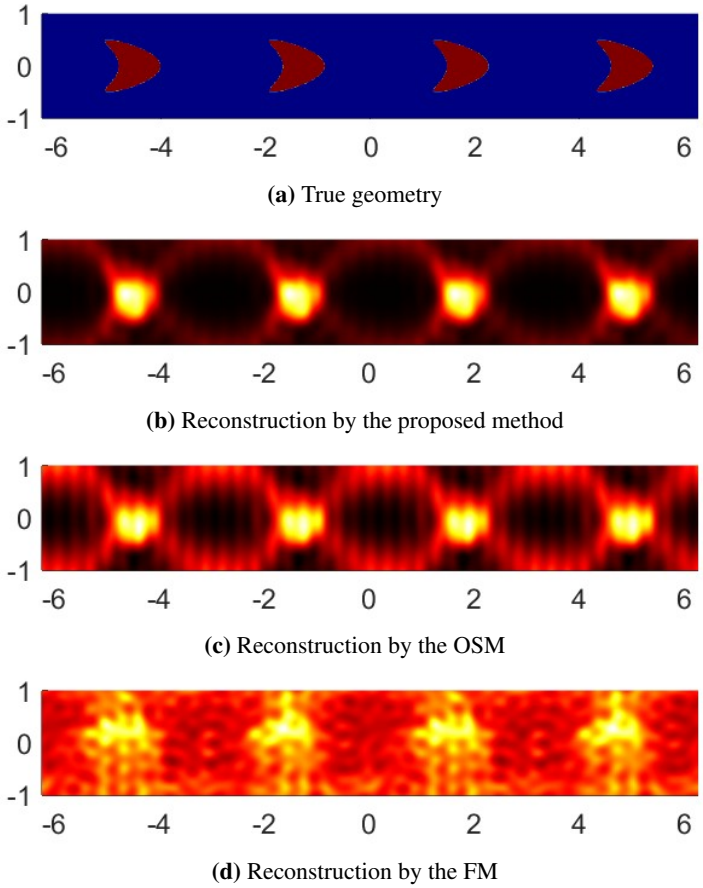

(a) True geometry

(b) Reconstruction by the proposed method

(c) Reconstruction by the OSM

(d) Reconstruction by the FM

Figure 5. Reconstructions by the proposed method, the OSM, and the FM for the isotropic aligned kites.

In all cases, the proposed imaging function outperforms the OSM. The FM simply fails because of a high level of noise and a lack of data. Note again that we aim to solve the inverse problem under a lack of data, which is extremely challenging. Nevertheless, the proposed method is able to provide reasonable results.

5.2. Results for anisotropic media

In this part, we present results for some anisotropic media. In this case, the medium is characterized by a 2×2 matrix-valued function $Q(x)$. In all examples, $Q(x)$ has the form

$$Q(x) = \begin{cases} \text{diag}(0.5, 0.25) & \text{if } x \in D, \\ 0 & \text{if } x \notin D, \end{cases}$$

where $\text{diag}(0.5, 0.25)$ is a 2×2 diagonal matrix whose first and second diagonal entries are 0.5 and 0.25, respectively. We consider the same geometries as in the isotropic case. Figures 6–9 show the reconstructions of the proposed imaging function versus those of the OSM and FM. The comparison result is similar to the isotropic case, with the proposed method outperforming both the OSM and FM.

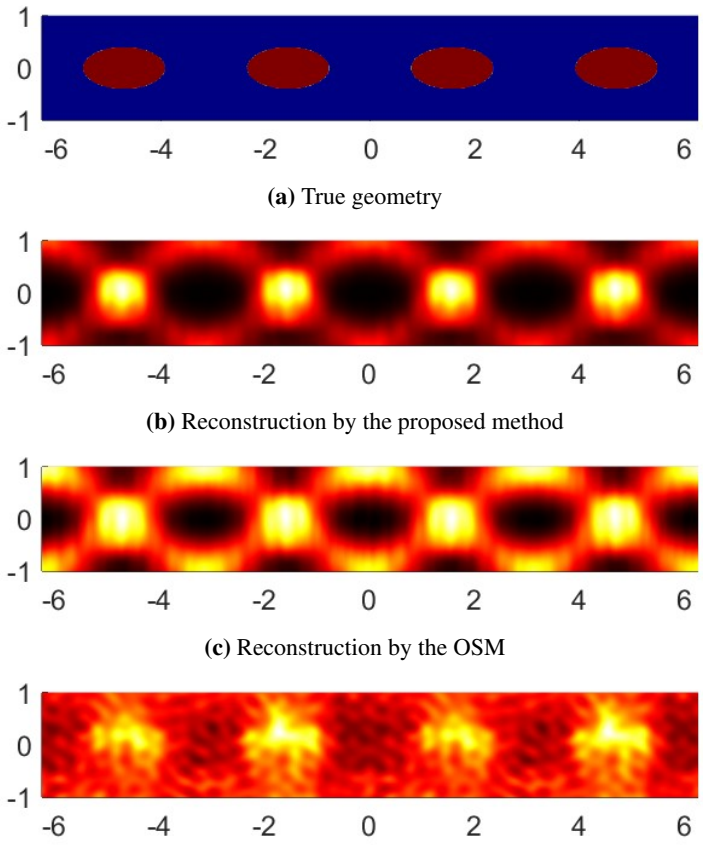

(a) True geometry

(b) Reconstruction by the proposed method

(c) Reconstruction by the OSM

(d) Reconstruction by the FM

Figure 6. Reconstructions by the proposed method, the OSM, and the FM for the anisotropic aligned ellipses.

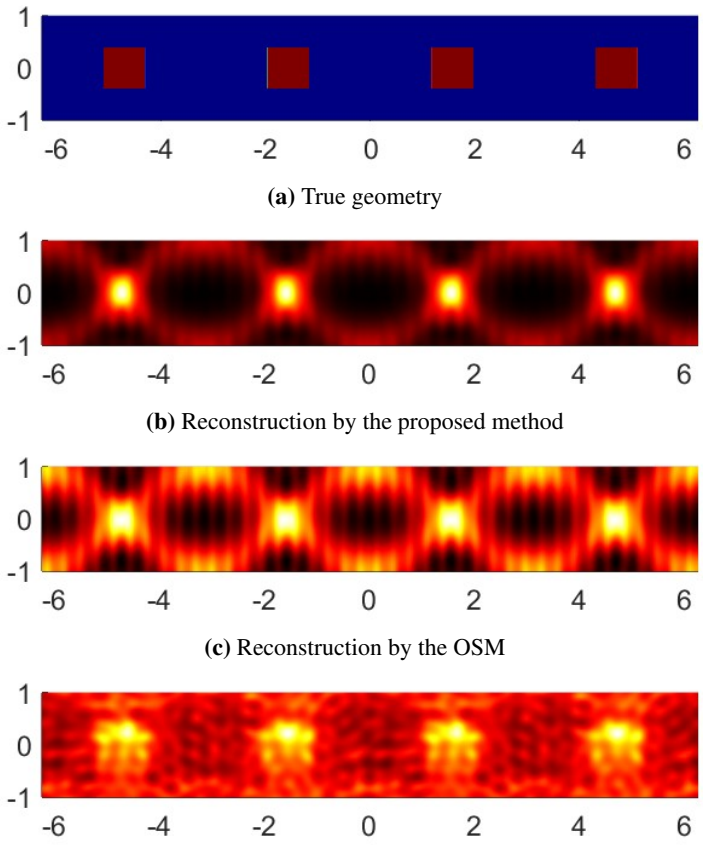

(a) True geometry

(b) Reconstruction by the proposed method

(c) Reconstruction by the OSM

(d) Reconstruction by the FM

Figure 7. Reconstructions by the proposed method, the OSM, and the FM for the anisotropic aligned squares.

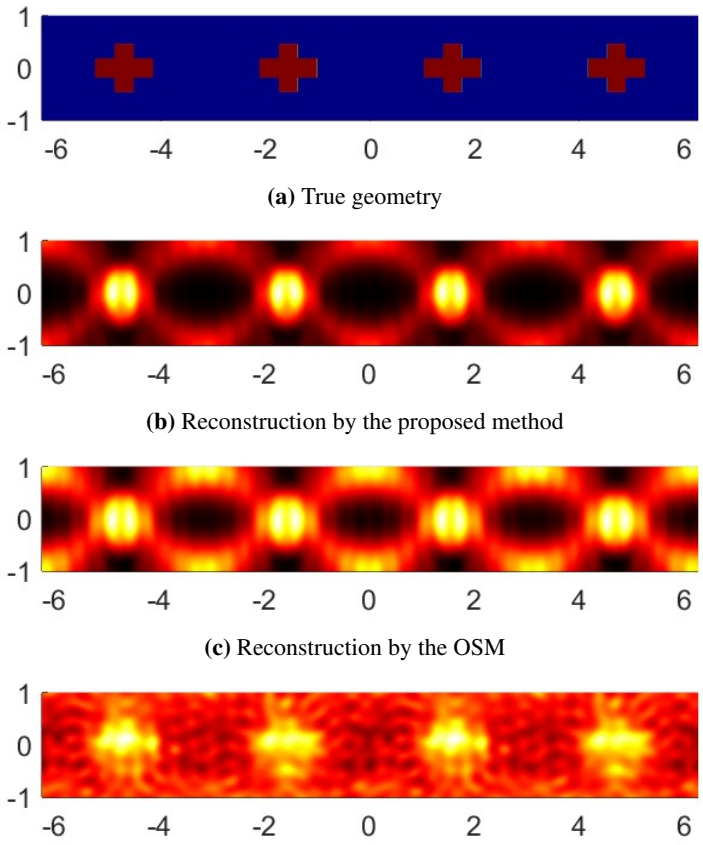

(a) True geometry

(b) Reconstruction by the proposed method

(c) Reconstruction by the OSM

(d) Reconstruction by the FM

Figure 8. Reconstructions by the proposed method, the OSM, and the FM for the anisotropic aligned crosses.

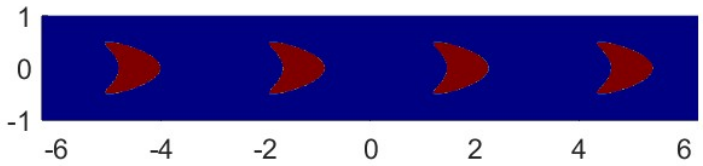

(a) True geometry

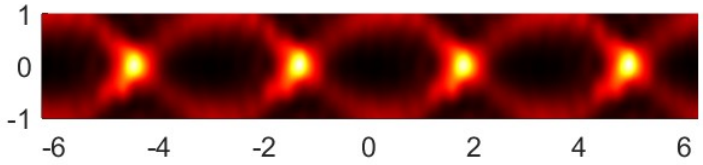

(b) Reconstruction by the proposed method

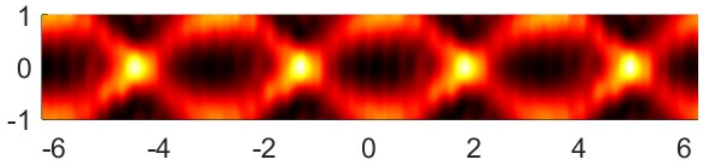

(c) Reconstruction by the OSM

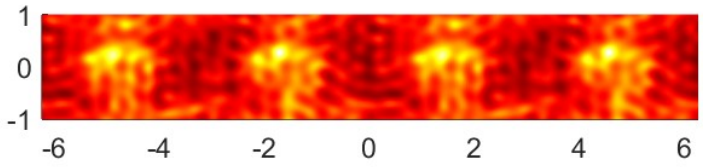

(d) Reconstruction by the FM

Figure 9. Reconstructions by the proposed method, the OSM, and the FM for the anisotropic aligned kites.

Use of AI tools declaration

The authors declare they have not used Artificial Intelligence (AI) tools in the creation of this article.

Acknowledgments

This research is partially supported by the National Science Foundation Grants DMS-2208293 and DMS-2243854.

Conflict of interest

The authors declare there are no conflicts of interest.

References

1. W. Dorfler, A. Lechleiter, M. Plum, G. Schneider, C. Wieners, *Photonic Crystals: Mathematical Analysis and Numerical Approximation*, Springer, 2012. https://doi.org/10.1007/978-3-0348-0113-3
2. T. Arens, N. Grinberg, A complete factorization method for scattering by periodic structures, *Computing*, **75** (2005), 111–132. https://doi.org/10.1007/s00607-004-0092-0
3. G. Bao, T. Cui, P. Li, Inverse diffraction grating of Maxwell's equations in biperiodic structures, *Opt. Express*, **22** (2014), 4799–4816. https://doi.org/10.1364/OE.22.004799
4. F. Cakoni, H. Haddar, T. P. Nguyen, New interior transmission problem applied to a single Floquet–Bloch mode imaging of local perturbations in periodic media, *Inverse Probl.*, **35** (2019), 015009. https://doi.org/10.1088/1361-6420/aaecfd
5. H. Haddar, T. P. Nguyen, Sampling methods for reconstructing the geometry of a local perturbation in unknown periodic layers, *Comput. Math. Appl.*, **74** (2017), 2831–2855. https://doi.org/10.1016/j.camwa.2017.07.015
6. A. Lechleiter, D. L. Nguyen, Factorization method for electromagnetic inverse scattering from biperiodic structures, *SIAM J. Imag. Sci.*, **6** (2013), 1111–1139. https://doi.org/10.1137/120903968
7. D. L. Nguyen, The factorization method for the Drude-Born-Fedorov model for periodic chiral structures, *Inverse Probl. Imaging*, **10** (2016), 519–547. https://doi.org/10.3934/ipi.2016010
8. D. L. Nguyen, T. Truong, Imaging of bi-anisotropic periodic structures from electromagnetic near field data, *J. Inverse Ill-Posed Probl.*, **30** (2022), 205–219. https://doi.org/10.1515/jiip-2020-0114
9. T. P. Nguyen, Differential imaging of local perturbations in anisotropic periodic media, *Inverse Probl.*, **36** (2020), 034004. https://doi.org/10.1088/1361-6420/ab2066
10. K. Sandfort, *The Factorization Method for Inverse Scattering from Periodic Inhomogeneous Media*, Ph.D thesis, Karlsruher Institut für Technologie, 2010. https://doi.org/10.5445/KSP/1000019400
11. J. Yang, B. Zhang, R. Zhang, A sampling method for the inverse transmission problem for periodic media, *Inverse Probl.*, **28** (2012), 035004. https://doi.org/10.1088/0266-5611/28/3/035004
12. A. Kirsch, N. Grinberg, *The Factorization Method for Inverse Problems*, Oxford University Press, 2008. https://doi.org/10.1093/acprof:oso/9780199213535.001.0001
13. D. Colton, A. Kirsch, A simple method for solving inverse scattering problems in the resonance region, *Inverse Probl.*, **12** (1996), 383–393. https://doi.org/10.1088/0266-5611/12/4/003
14. A. Kirsch, Characterization of the shape of a scattering obstacle using the spectral data of the far field operator, *Inverse Probl.*, **14** (1998), 1489–1512. https://doi.org/10.1088/0266-5611/14/6/009
15. X. Jiang, P. Li, Inverse electromagnetic diffraction by biperiodic dielectric gratings, *Inverse Probl.*, **33** (2017), 085004. https://doi.org/10.1088/1361-6420/aa76b9
16. R. Griesmaier, Multi-frequency orthogonality sampling for inverse obstacle scattering problems, *Inverse Probl.*, **27** (2011), 085005. https://doi.org/10.1088/0266-5611/27/8/085005

17. I. Harris, D. L. Nguyen, Orthogonality sampling method for the electromagnetic inverse scattering problem, *SIAM J. Sci. Comput.*, **42** (2020), B722–B737. https://doi.org/10.1137/19M129783X

18. K. Ito, B. Jin, J. Zou, A direct sampling method to an inverse medium scattering problem, *Inverse Probl.*, **28** (2012), 025003. https://doi.org/10.1088/0266-5611/28/2/025003

19. R. Potthast, A study on orthogonality sampling, *Inverse Probl.*, **26** (2010), 074015. https://doi.org/10.1088/0266-5611/26/7/074015

20. D. L. Nguyen, K. Stahl, T. Truong, A new sampling indicator function for stable imaging of periodic scattering media, *Inverse Probl.*, **39** (2023), 065013. https://doi.org/10.1088/1361-6420/acce5f

21. D. L. Nguyen, T. Truong, A stable imaging functional for anisotropic periodic media in electromagnetic inverse scattering, *SIAM J. Appl. Math.*, **84** (2024), 1631–1657. https://doi.org/10.1137/23M1577080

22. A. S. Bonnet-Bendhia, F. Starling, Guided waves by electromagnetic gratings and non-uniqueness examples for the diffraction problem, *Math. Methods Appl. Sci.*, **17** (1994), 305–338. https://doi.org/10.1002/mma.1670170502

23. D. L. Colton, R. Kress, *Inverse Acoustic and Electromagnetic Scattering Theory*, 2nd edition, Springer, 1998. https://doi.org/10.1007/978-3-662-03537-5

24. A. Lechleiter, D. L. Nguyen, Volume integral equations for scattering from anisotropic diffraction gratings, *Math. Methods Appl. Sci.*, **36** (2013), 262–274. https://doi.org/10.1002/mma.2585

25. A. Lechleiter, D. L. Nguyen, A trigonometric Galerkin method for volume integral equations arising in TM grating scattering, *Adv. Comput. Math.*, **40** (2014), 1–25. https://doi.org/10.1007/s10444-013-9295-2

AIMS Press